

Cite this: *Chem. Sci.*, 2023, 14, 9427

All publication charges for this article have been paid for by the Royal Society of Chemistry

A natural polyphenol activates and enhances GPX4 to mitigate amyloid- β induced ferroptosis in Alzheimer's disease†

Prayasee Baruah,[‡] Hariharan Moorthy,[‡] Madhu Ramesh,[‡] Dikshaa Padhi and Thimmaiah Govindaraju^{‡*}

Ferroptosis, an iron-dependent cell death, plays a crucial role in the pathology of Alzheimer's disease (AD). Several characteristics of AD, including excessive iron accumulation, elevated lipid peroxide and reactive oxygen species (ROS) levels, and decreased glutathione peroxidase 4 (GPX4) levels, align with the features of ferroptosis. While traditional methods of inhibiting ferroptosis have centered on chelating Fe and trapping radicals, therapeutic strategies that modulate the GPX4 axis to mitigate ferroptosis in AD are yet to be explored. This report introduces naturally occurring polyphenols (PPs) as dual-acting therapeutic agents to synergistically alleviate ferroptosis and AD. The mechanisms of action encompass modulation of amyloid and tau cascade, reduction of oxidative stress, mitochondrial rescue, and inhibition of ferroptosis. For the first time, we show that a single multifunctional molecule, tannic acid (TA) binds at the activator site of GPX4, augmenting both its activity and cellular levels, providing a conceptually innovative and integrated approach for treating AD via the GPX4–ferroptosis axis. The ability of TA to enhance GPX4 levels under conditions of AD pathology opens up newer promising therapeutic avenues for combating the crosstalk between ferroptosis and AD.

Received 7th May 2023
Accepted 19th August 2023

DOI: 10.1039/d3sc02350h

rsc.li/chemical-science

Introduction

AD is a prevalent neurodegenerative disorder and the most common form of dementia, characterized by a progressive decline in memory and cognitive function.^{1,2} Despite significant research progress, the understanding of its etiology remains limited. The primary factors contributing to AD include the deposition of A β plaques and tau neurofibrillary tangles (NFTs), decline in the neurotransmitter acetylcholine, synaptic dysfunction, and neurodegeneration in the brain.^{3–5} Metal dys-homeostasis, oxidative stress, and biomolecular and mitochondrial damage have been implicated in AD pathophysiology, wherein the accumulation of metal ions (Cu, Fe, and Zn) exacerbates AD pathology by accelerating the aggregation of A β and tau.^{6–10} Currently prescribed medications for AD, including cholinesterase inhibitors and *N*-methyl-D-aspartate receptor antagonists provide symptomatic relief and do little to slow the disease progression. While there are no fully approved treatments targeting the core pathology of AD, recently, two monoclonal antibody-based drugs (aducanumab and lecanemab)

targeting the A β ₄₂ cascade have been given conditional approval.^{11,12}

Ferroptosis, an iron-regulated cell death, has recently garnered attention in etiological research and treatment due to its involvement in various disorders.^{13,14} Intracellular iron levels are critical factors in ferroptosis. Elevated iron levels initiate the Fenton-type reaction, which increases non-enzymatic lipid peroxidation and drives ferroptotic cell death. Iron also facilitates enzymatic lipid peroxidation by serving as a cofactor for specific lipoxygenase (LOX) enzymes. LOX, a non-heme iron-containing dioxygenase family, catalyzes polyunsaturated fatty acid (PUFA) oxidation to generate hydroperoxyl derivatives.¹⁴ Conversely, cells with low iron levels or robust iron sequestration mechanisms may exhibit greater resistance to ferroptosis.¹⁵ However, the iron concentration threshold for initiating ferroptosis remains elusive. Research has also revealed that mitochondrial dysfunction, lipid peroxidation, and a decrease in the activity and levels of the antioxidant enzyme glutathione peroxidase 4 (GPX4) are associated with ferroptosis.^{16,17} GPX4, the master regulator of ferroptosis is known to reduce toxic lipid peroxides formed by the reaction of polyunsaturated fatty acids (PUFAs) with reactive oxygen species (ROS) to lipid alcohol.¹³ GPX4 activity is significantly influenced by the amount of iron present in cells. The availability of GPX4's cofactor, glutathione (GSH), which aids in the neutralization of lipid hydroperoxides, is necessary for the enzyme's function. High levels of iron can lead to the generation of excess reactive oxygen species (ROS)

Bioorganic Chemistry Laboratory, New Chemistry Unit, The School of Advanced Materials (SAMat), Jawaharlal Nehru Centre for Advanced Scientific Research (JNCASR), Bengaluru 560064, Karnataka, India. E-mail: tgraju@jncasr.ac.in

† Electronic supplementary information (ESI) available. See DOI: <https://doi.org/10.1039/d3sc02350h>

‡ Equal contribution.

via the Fenton-type reaction, which involves iron-catalyzed production of hydroxyl radicals from hydrogen peroxide. These ROS can overwhelm GSH/GPX4's antioxidant capacity, leading to increased lipid peroxidation and potential inactivation of the enzyme. Ferroptosis can also manifest independently of the GPX4 axis. For instance, tumor protein 53 (TP53) drives ferroptosis without GPX4 inhibition *via* the cysteine/glutamate antiporter pathway.¹⁸ ML210-triggered ferroptosis led by cytochrome P450 reductase (POR) can occur in the absence of GPX4.¹⁹ Ferroptosis suppressor protein FSP1 has also emerged as a regulator of ferroptosis, which can function both in conjunction with and independent of GPX4. These findings highlight the complexity of ferroptosis and its involvement with various molecular machineries.

While ferroptosis is being explored as a therapeutic route to annihilate tumours, it has been found to play an antagonistic role in several neurological conditions, including AD, hemorrhagic stroke, ischemic stroke, Parkinson's disease, and Huntington's disease.^{20,21} Patients with mild cognitive impairment (MCI) and high amyloid plaque loads exhibit an increase in cortical iron accumulation, which heightens the risk of AD.²² Ferroptosis, a form of regulated cell death, has been implicated in the development of AD, characterized by iron-driven lipid peroxidation and glutamate excitotoxicity in the brain tissues of AD patients and models. Cerebrospinal fluid (CSF) ferritin levels have been found to be inversely associated with MCI and AD, with the Alzheimer's risk allele APOE-ε4 increasing ferritin levels, indicating that iron imbalance may be a risk factor for AD.²³ Ferroptosis inhibitors have been shown to protect neurons and restore cognitive function in animal models of stroke.²⁴ In mice, GPX4 knockout resulted in age-dependent neurodegenerative changes and significant neuronal loss.²⁵ In another study, treatment with Aβ₄₂ increased tissue Fe content and ferritin levels while decreasing GPX4 levels in the hippocampus, suggesting that Aβ₄₂ may directly induce ferroptosis in neurons.²⁶ This complex interplay between iron imbalance and ferroptosis highlights their contributions to neuronal death in AD pathogenesis and holds potential for therapeutic insights.

Oxidative stress, induced by ROS, is a critical factor in the development of AD and ferroptosis. Antioxidants that can neutralize ROS show potential as dual therapeutic targets. Hydroxylated chalcones have been reported as dual-functional inhibitors of Aβ₄₂ aggregation and ferroptosis with the potential treatment for AD.²⁷ Despite the established link between AD and ferroptosis, there are very few dual-acting therapeutics that target the complex causes of both conditions. The development of ferroptosis inhibitors has mainly focused on Fe-chelation and antioxidant capability; however, the activation of GPX4, an important factor in combating ferroptosis, remains largely unexplored. GPX4 protein synthesis is energetically demanding with low efficiency, and therefore, molecules that can activate and elevate GPX4 might be the key to modulate oxidative stress implicated in chronic disorders.²⁸ There is an unmet need for the development of multifunctional molecules that target both ferroptosis and AD and synergistically enhance and activate the natural antioxidant mechanism involving GPX4 to mitigate the complex pathology of ferroptosis in AD.

In this work, a set of structurally correlated natural polyphenols (PPs) were screened for their therapeutic ability towards AD and ferroptosis. Tannic acid (TA) was identified as a dual-acting therapeutic against AD and ferroptosis by modulating Aβ₄₂ and tau cascade, metal chelation, reduction of oxidative stress, mitochondrial rescue, binding and activation of GPX4 and inhibition of ferroptosis (Fig. 1A). Surprisingly, TA was found not only to enhance the GPX4 activity but also to increase GPX4 levels in cells. To the best of our knowledge, this is the first report to identify a single molecule as both a GPX4 activator and enhancer to mitigate ferroptosis in the context of AD pathology. Besides, TA was found to activate Nrf2, which is known to regulate ferroptosis in neuronal cells. The combined approach of Nrf2–GPX4 activation and ferroptosis inhibition, along with modulation of Aβ₄₂ and tau pathways, presents a new therapeutic avenue for the treatment of multifactorial AD.

Results

Fe-binding interaction of PPs

As ferroptosis is an Fe-dependent cell death, Fe-chelators are considered to be viable and promising inhibitors of ferroptosis. A set of PPs, mostly containing catechol and gallate moieties, were evaluated for their Fe-chelation ability. The screened PPs included gallic acid (GA), epigallocatechin gallate (EGCG), tannic acid (TA), ellagic acid (EA), genistein (GEN), syringic acid (SA), methyl gallate (MeG), 4-hydroxyflavone (4-HF), and 2-



Fig. 1 Schematic representation of the mechanism of action of TA. (A) Ferroptosis is mediated by an accumulation of free Fe within cells. GPX4 converts toxic lipid peroxides into lipid alcohols. TA inhibits RSL3 and Aβ₄₂–Fe induced ferroptosis through Fe-chelation, antioxidant mechanisms, modulation of Aβ₄₂ and tau aggregation, and GPX4 and Nrf2 activation. TA: tannic acid, GPX4: glutathione peroxidase 4, PUFA: polyunsaturated fatty acid, Nrf2: nuclear factor erythroid 2-related factor 2, RSL3: RAS-selective lethal 3, LIP: labile iron pool. (B) Structures of polyphenols (PPs) screened in this study.



hydroxyflavone (2-HF) (Fig. 1B). The strength of interaction between these PPs and Fe^{3+} was determined using UV-vis absorption spectroscopy in HEPES buffer (10 mM, pH = 7.4). Upon addition of FeCl_3 (1 to 10 μM), the UV-vis absorption spectra of the PPs (6 μM) showed an increase in absorbance, with the maximum increase observed for TA (Fig. 2A). The data were fitted to the Benesi–Hildebrand equation to determine the binding constant (K_B). TA, which contains five gallic acid moieties, exhibited the highest Fe-chelation ability among all PPs with a K_B value of $6.64 \times 10^5 \text{ M}^{-1}$ compared to $5.1 \times 10^5 \text{ M}^{-1}$ and $4.2 \times 10^3 \text{ M}^{-1}$ for EGCG and GA, respectively (Fig. 2B). The binding constants for MeG, GEN, EA and 2-HF were found to be

much lower than that of TA as listed (2.7×10^3 , 1.5×10^4 , 1.9×10^5 , and $9.8 \times 10^3 \text{ M}^{-1}$, respectively) in Table S1†

To assess the selectivity for Fe, TA was titrated against other metal ions implicated in AD (Cu^{2+} , Zn^{2+} , and Al^{3+}) and common biometal ions (Na^+ , K^+ , and Ca^{2+}). The study revealed that the binding constant of TA for Fe ($6.64 \times 10^5 \text{ M}^{-1}$) was two orders of magnitude higher than that for Cu^{2+} , Zn^{2+} , and Al^{3+} ($1.63 \times 10^3 \text{ M}^{-1}$, $2.9 \times 10^3 \text{ M}^{-1}$, and $9.9 \times 10^3 \text{ M}^{-1}$, respectively), while there was no significant binding interaction with Na^+ , K^+ , and Ca^{2+} (Fig. S1 and Table S2†). The ability of PPs to chelate Fe^{3+} varied in the order of TA > EGCG > EA > GA > MeG > GEN > 4-HF > 2-HF > SA (Fig. S2A–H and Table S2†). Furthermore, the formation of the TA- Fe^{3+} complex was confirmed by the appearance of a new peak at 580 nm (Fig. S3†). The data obtained from Job's plot revealed 1 : 4 binding of TA : Fe^{3+} which accounts for the high affinity of TA to Fe^{3+} . These absorption-based binding studies were further supported by isothermal titration calorimetry (ITC) experiments performed with TA, the strongest Fe-chelator. ITC experiments (Fig. S4†) revealed that the titration of TA with FeCl_3 resulted in an endothermic reaction, revealing binding between the two components, with a dissociation constant (K_d) of $31.1 \pm 3.2 \mu\text{M}$. The interaction between TA and Fe^{3+} was found to be spontaneous ($\Delta G = -6.73 \text{ kcal mol}^{-1}$) and enthalpically favoured ($\Delta H = -77.9 \pm 22.3 \text{ kcal mol}^{-1}$) as revealed by the K_d and ΔG values implying a strong interaction.

Antioxidant effect and inhibition of lipid peroxidation

α -Diphenyl- β -picrylhydrazyl (DPPH), 2,2'-azino-bis(3-ethylbenzothiazoline-6-sulfonic acid) (ABTS), and ferric ascorbate assays were performed to evaluate the antioxidant activities of the potent Fe-chelators TA and EGCG, along with GA, which is the primary metal chelating and antioxidant moiety.^{29,30} DPPH and ABTS form stable free radicals that can be used to determine the free radical scavenging capacity of antioxidants. TA and EGCG exhibited better radical scavenging abilities compared to ascorbate, a control used in the study (Fig. S5A and B†). The ability of PPs to redox-silence Fe^{3+} and quench excessive ROS was evaluated using the Ferric ascorbate assay in PBS buffer (10 mM, pH = 7.4) with FeCl_3 (20 μM) (Fig. 2C).³¹ TA showed a reduction in emission at 452 nm in a concentration-dependent manner (0 to 20 μM), suggesting that it arrests Fe^{3+} and stabilizes the redox dormant state, and scavenges free radicals (Fig. 2D). At the highest concentration of 20 μM , the quenching of ROS by TA was ~80%. Interestingly, a similar experiment performed in the presence of $\text{A}\beta_{42}$ to mimic AD conditions revealed that TA can effectively bind and arrest the Fe^{3+} redox process thereby quenching ROS production (Fig. 2E). EGCG was also found to be effective as an antioxidant, albeit with slightly less activity compared to TA (Fig. S5C and D†). The extent of protein oxidation under oxidative stress can be approximated by measuring protein carbonyl levels. The protective effect of PPs against the oxidation of bovine serum albumin (BSA) was evaluated using a $\text{Fe}^{2+} + \text{H}_2\text{O}_2$ redox system that generates ROS *in situ* and simulates an environment of Fe-mediated oxidative stress similar to ferroptosis conditions.



Fig. 2 Fe-chelation and antioxidant studies of PPs. (A) UV-visible spectra of TA in the presence of increasing concentrations of FeCl_3 . (B) The graph was derived by fitting the data from (A) using the Benesi–Hildebrand equation. (C) Radical scavenging of PPs monitored by the Ferric ascorbate assay, and concentration-dependent radical scavenging of TA (D) and TA in the presence of $\text{A}\beta_{42}$ (E). (F) Inhibition of protein oxidation by PPs monitored by the 2,4-dinitrophenylhydrazine (DNPH) assay. (G) Inhibition of lipid peroxidation by PPs monitored by the thiobarbituric acid reactive substance (TBARS) assay and (H) concentration-dependent inhibition of lipid peroxidation by TA and EGCG.



Treatment with **TA** (20 μM) and **EGCG** (20 μM) reduced protein oxidation by 30% and 35%, respectively (Fig. 2F). The DNPH assay was performed using DFO and Ferrostatin-1, in addition to **TA**. **TA** demonstrated comparable, albeit slightly superior, efficacy in inhibiting protein oxidation compared to Ferrostatin-1, while the effect of the iron chelator DFO was less than that of all other compounds studied (Fig. S6A†).

Next, a lipid peroxidation assay (TBARS) was performed using α -phosphatidylcholine as a model lipid and the $\text{Fe}^{2+} + \text{H}_2\text{O}_2$ redox system to measure the extent of lipid peroxidation under ferroptosis conditions.³² The peroxidation of α -phosphatidylcholine with $\text{Fe}^{2+} + \text{H}_2\text{O}_2$ was used as a control (100%) and the percentage inhibition of lipid peroxidation in the presence of **TA** (20 μM) and **EGCG** (20 μM) was found to be 42% and 40%, respectively (Fig. 2G). The concentration-dependent plot of lipid peroxidation in the presence of **TA** and **EGCG** revealed their excellent peroxidation inhibition activity, which can be attributed to their synergistic Fe-chelation and radical trapping mechanism (Fig. 2H). The extent of lipid peroxidation was also compared with that of known ferroptosis inhibitors, DFO and Ferrostatin-1. The assay was performed using two concentrations (10 and 20 μM) of all compounds. **TA** and Ferrostatin-1 exhibited almost similar potency in inhibiting lipid peroxidation, while the iron chelator DFO showed only a marginal reduction in lipid peroxidation compared to the other compounds (Fig. S6B†).

Modulation of Fe-independent and -dependent $\text{A}\beta_{42}$ and tau aggregation

The ability of PPs to modulate the Fe-independent and -dependent aggregation propensity of $\text{A}\beta_{42}$ was evaluated.³² Aggregation-dependent Thioflavin T (ThT) fluorescence data revealed that **EGCG** and **TA** exhibited superior activity among all the PPs, with 44% and 35% aggregation inhibition at a concentration of 20 μM (Fig. 3A). The lag time (T_{lag}) for $\text{A}\beta_{42}$ aggregation was found to be 9.2 h with a first-order aggregation rate constant (κ) of 0.51 h^{-1} . The increasing concentrations of **TA** and **EGCG** increased T_{lag} and decreased κ , indicating a significant delay in $\text{A}\beta_{42}$ aggregation (Fig. 3B, S8A and Table S2†). At a 1 : 5 ratio ($\text{A}\beta_{42}$: PP), **EGCG** exhibited relatively better inhibitory efficiency (95%) compared to **TA** (82%). The effect of Fe on $\text{A}\beta_{42}$ aggregation was studied due to the key role of Fe-homeostasis in the etiology of AD. $\text{A}\beta_{42}$ with Fe^{3+} in a 1 : 1 ratio decreased T_{lag} to 8.72 h compared to pristine $\text{A}\beta_{42}$ (9.2 h), while κ increased from 0.51 h^{-1} to 0.72 h^{-1} (Fig. 3C). Interestingly, while **EGCG** showed marginally better results for Fe-independent aggregation, the inhibition propensities of **TA** and **EGCG** were comparable in the case of Fe-induced aggregation possibly due to the ability of **TA** to sequester Fe^{3+} (Tables S3 and S4†). At a 1 : 5 ratio, **TA** and **EGCG** showed T_{lag} values of 10.12 h and 10.9 h, with κ values of 0.20 h^{-1} and 0.17 h^{-1} , respectively (Fig. 3D and S7B†). To verify that the affinity of Fe to **TA** was higher than that for $\text{A}\beta$, ITC studies were performed for $\text{A}\beta$ -Fe complexation. The dissociation constant of the $\text{A}\beta$ -Fe complex ($286 \pm 19.7 \mu\text{M}$) (Fig. S8†) was found to be much higher than that of the **TA**-Fe ($31 \pm 3.2 \mu\text{M}$) complex (Fig. S4†), which supports that **TA** might be able to sequester Fe from the $\text{A}\beta$ -Fe complex.

The ability of PPs to modulate arachidonic acid-induced tau (5 μM) aggregation was monitored using Thioflavin T (ThT) fluorescence kinetics (Fig. 3E). **EGCG** and **TA** showed 53% and 46% aggregation inhibition, respectively, at a concentration of 20 μM . **TA** and **EGCG** exhibited concentration-dependent activity with the highest inhibition of 70% and 81%, respectively, at a ratio of 1 : 5 up to 2.5 h after which no further increase in ThT fluorescence was observed (Fig. 3F and S8C†). An experiment was performed to investigate the impact of Fe^{3+} on the aggregation of tau induced by AA. Tau was incubated with FeCl_3 in a 1 : 1 ratio and the aggregation kinetics was monitored. The results indicated that the presence of Fe^{3+} did not significantly alter the aggregation kinetics of tau (Fig. S9†).

Molecular docking was performed to gain insights into the interaction of compounds with $\text{A}\beta_{42}$ and tau. Docking studies of **TA** and **EGCG** with $\text{A}\beta_{42}$ monomers and fibrils (PDB ID 1Z0Q and 2BEG of <https://www.rcsb.org>)^{33,34} showed negative free energy change (ΔG) values, indicating favorable interaction through spontaneous binding to the $\text{A}\beta_{42}$ monomer (-38 kJ mol^{-1} and -34 kJ mol^{-1}) and fibrillar aggregates (-39 kJ mol^{-1} and -36 kJ mol^{-1}), respectively (Fig. S10A, B, S11A and B†). The elongated lag phase observed in the ThT kinetics study suggested the influence of **TA** and **EGCG** on both the monomeric and fibrillar forms of $\text{A}\beta_{42}$, which was confirmed by the docking studies. Molecular docking of **TA** and **EGCG** was also performed with tau protofibrils (PDB ID 5O3T of <https://www.rcsb.org>).³⁵ The estimated negative ΔG values of **TA** and **EGCG** ($-34.1 \text{ kJ mol}^{-1}$ and 33.3 kJ mol^{-1} , respectively) indicated thermodynamically favored interactions of these PPs with tau (Fig. S12A†).

Activation of GPX4 and reversal of its RSL3-induced inhibition

A deficiency of GPX4 increases the susceptibility of cells to ferroptosis.^{36,37} Despite their significance, reports of small molecule activators of GPX4 are rare, while inhibitors of GPX4 such as RAS-selective lethal 3 (RSL3) and ML-162, that induce ferroptosis by inhibiting GPX4, are well documented.^{38,39} RSL3 binds to the inhibitor site of GPX4 and suppresses its activity while activating nuclear factor kappa B (NF- κ B), leading to ferroptosis and cell death.⁴⁰ Molecular docking was performed to explore the potential interaction of **TA** and **EGCG** binding to GPX4 (PDB ID 2OBI of <https://www.rcsb.pdb>). GPX4 has two distinct sites: a substrate binding site and an allosteric site.^{41,42} Small molecule binding to the former (inhibitor site) serves as an inhibitor while binding to the latter (activating site) is predicted to enhance GPX4 activity (Fig. 4A). **TA** was found to bind to the activator site of GPX4, while **EGCG** interacts at an alternate site that did not conform with either activation or inhibition sites of GPX4. Docking studies were performed with GPX4 inhibitor RSL3 and GPX4 activator PKUMDL-LC-102 (Fig. 4A).⁴² The results showed that RSL3 bound to the inhibition site while PKUMDL-LC-102 bound to the activator site, similar to **TA**. The GPX4 activator PKUMDL-LC-102 was found to be surrounded by acidic residues D21 and D23 and apolar residues V98, F100, and M102 at the allosteric activator site (Fig. 4A). Interestingly, **TA** also bound to the activator site through specific interactions with the same set of





Fig. 3 Screening of PPs for their ability to inhibit $A\beta_{42}$ and tau aggregation monitored using ThT assay ($\lambda_{\text{ex}} = 444$ nm and $\lambda_{\text{em}} = 484$ nm). $[A\beta_{42}] = 10$ μM , $[\text{Tau}] = 5$ μM . (A) Effect of PP on $A\beta_{42}$ aggregation. $[\text{PP}] = 20$ μM . (B) Kinetics of $A\beta_{42}$ aggregation in the presence of increasing concentrations of TA (10 to 50 μM). (C) Comparison of kinetic curves of $A\beta_{42}$ aggregation and Fe-induced $A\beta_{42}$ aggregation. $[\text{FeCl}_3] = 10$ μM . (D) Kinetics of Fe-induced $A\beta_{42}$ aggregation in the presence of an increasing concentration of TA (10 to 50 μM). (E) Screening of PPs for their ability to inhibit AA-induced tau aggregation. $[\text{PP}] = 20$ μM , and $[\text{AA}] = 185$ μM . (F) Kinetics of tau aggregation in the presence of increasing concentrations of TA (5 to 25 μM). AA: arachidonic acid.

amino acid residues. Independent docking of TA and PKUMDL-LC-102 to GPX4 showed that the binding interaction of TA was favored over that of PKUMDL-LC-102 with ΔG values of -63.1 kJ mol^{-1} and -33.0 kJ mol^{-1} respectively, indicating that TA is a strong GPX4 activator. These results led to experimental verification of the TA effect on GPX4 activity and its ability to reverse RSL3-inhibited GPX4 activity.

The effect of TA on GPX4 activity was assessed using a GPX4 inhibitor screening assay kit (Cayman Chemical, USA). In this assay, the consumption of NADPH by GPX4 was used to monitor enzymatic activity. A steady decrease in absorbance over time provided a reference kinetic curve for GPX4 activity. Incubation of GPX4 with RSL3 (20 μM) for 60 min inhibited GPX4 activity by 22%. However, at a concentration of 20 μM , both TA and EGCG were able to reverse the RSL3-induced inhibition by 12.3% and 9.5%, respectively (Fig. 4B). TA increases GPX4 activity by binding to its activation site. In contrast, EGCG does not bind to the GPX4 activation site but instead inhibits the binding of RSL3 to GPX4 (Fig. S13[†]). The half maximal inhibitory concentration (IC_{50}) value of RSL3 was calculated by monitoring its concentration-dependent inhibition of GPX4 activity (10 μM to 50 μM) and was found to be 17.17 ± 0.17 μM (Fig. 4C and D). This IC_{50} value for RSL3 was calculated independently and in the presence of TA. The addition of 20 μM of TA to the reaction mixture modulated the IC_{50} value of RSL3 from 17.17 ± 0.17 μM to 29.98 ± 1.09 μM , indicating that TA can reduce RSL3-induced GPX4 inhibition (Fig. 4E and F). EGCG (20 μM) showed a relatively lower ability to restore intrinsic enzyme activity upon

RSL3-induced GPX4 inhibition, changing the IC_{50} value to 21.01 ± 0.47 μM (Fig. 5B). TA was able to revert RSL3-induced GPX4 activity in a concentration-dependent manner (Fig. S14[†]). The docking results demonstrated the ability of TA to bind to the activation site of GPX4. This, coupled with its effectiveness in reversing RSL3-induced GPX4 inhibition, led us to investigate whether TA could directly function as a GPX4 activator. Our data showed that treatment of GPX4 with TA (0 to 100 μM) resulted in a concentration-dependent increase in enzyme activity. At a concentration of 100 μM TA, a 19% enhancement in GPX4 activity was observed (Fig. 4G). These results demonstrate that TA can not only restore GPX4 activity from RSL3-induced inhibition but also enhance its intrinsic activity. In contrast, EGCG did not function as a GPX4 activator, consistent with its binding at an alternate site in molecular docking analysis. A comprehensive analysis of all *in vitro* experiments identified TA as the most promising candidate for combating ferroptosis. This was primarily due to its ability to activate GPX4 accompanied by multifunctional activity. In contrast, EGCG demonstrated superior anti-amyloid and tau properties. Subsequent cell-based experiments were conducted with the lead PP candidates, TA and EGCG.

Rescue of ferroptosis-induced cell death

The viability of SH-SY5Y neuronal cells in the presence of lead PPs was evaluated using the 3-(4,5-dimethylthiazol-2-yl)-2,5-diphenyltetrazolium bromide (MTT) assay after 48 h of incubation. TA and EGCG were relatively non-toxic up to 60 μM , with



Fig. 4 Enzymatic activity of GPX4 in the presence of small molecules binding to inhibitor and activator sites. (A) GPX4 docking with RSL3 (inhibitor), PKUMDL-LC-102 (activator), and TA (novel activator). TA binds at the activator site of GPX4. (B) GPX4 activity modulation in the presence of RSL3 (20 μM) and RSL3 with TA and EGCG (20 μM). The graph displays the restoration of RSL3-inhibited enzyme activity by TA (C) GPX4 activity modulation in the presence of increasing concentrations of RSL3 and (D) the corresponding IC₅₀ plot. (E) GPX4 activity modulation in the presence of increasing RSL3 concentrations with 20 μM of TA and (F) the corresponding IC₅₀ plot. In the presence of TA, the IC₅₀ value of RSL3 changed from 17 μM to 30 μM. (G) The concentration-dependent effect of TA on GPX4 activity, demonstrating the enzyme-activating effect of TA. GPX4 activity in (B–G) was measured by monitoring the change in absorbance of NADPH upon its consumption in the assay.

cell viability exceeding 90% compared to untreated cells (Fig. S15[†]). To determine the ability of TA and EGCG to inhibit ferroptosis, SH-SY5Y cells were treated with RSL3 alone and in the presence of TA and EGCG. After 48 h incubation, RSL3 (500 nM) treatment reduced cell viability to 46%, compared to that of untreated cells (100%). Remarkably, treatment with TA and EGCG demonstrated rescue of neuronal cells in a concentration-dependent manner, with cell viability reaching 84% and 62%, respectively, at a concentration of 20 μM (Fig. 5A and B). A comparative study of TA with Ferrostatin-1 and DFO was performed to investigate the rescue ability from RSL3-induced ferroptotic cell death. Ferrostatin-1 showed almost 100% inhibition of ferroptosis at a low concentration of 10 μM. The effect of TA on rescuing RSL3-induced cell death was comparable to that of Ferrostatin-1 at a lower concentration. On the other hand, DFO did not demonstrate significant rescue from ferroptotic damage at the given concentration, despite having a stronger Fe chelating ability than TA. These data are very interesting, as they clearly indicate that Fe chelation alone cannot effectively alleviate ferroptotic stress. Though synthetic

molecule Ferrostatin-1 shows slightly better rescue ability from RSL3-induced ferroptosis, it is important to note that TA being a natural polyphenol available in high abundance and devoid of any synthetic modification represents a highly efficient, viable, and cost-effective approach for ferroptosis inhibition. GPX4 levels in cells treated with RSL3 alone and in the presence of TA and EGCG were monitored using an immunofluorescence assay. RSL3 (1 μM) treatment for 24 h reduced GPX4 levels to 83% compared to that in healthy cells (100%). Notably, TA (20 μM) and EGCG (20 μM) treatment resulted in the restoration of GPX4 levels in RSL3-treated cells to 96% and 91%, respectively, signifying recovery from ferroptosis (Fig. 5D and S16[†]). Furthermore, to validate these results, western blot analysis was performed to quantify GPX4 levels. GPX4 levels were reduced to 73% compared to that in control cells (100%) upon treatment with RSL3 (1 μM) (Fig. 5E, F and S20[†]). Notably, upon treatment with TA (20 μM), complete restoration of GPX4 levels were seen.

An elevated LIP is a hallmark of ferroptosis, catalyzing lipid peroxidation and leading to cellular death.⁴³ To measure LIP in cells treated with RSL3 alone and in the presence of TA and



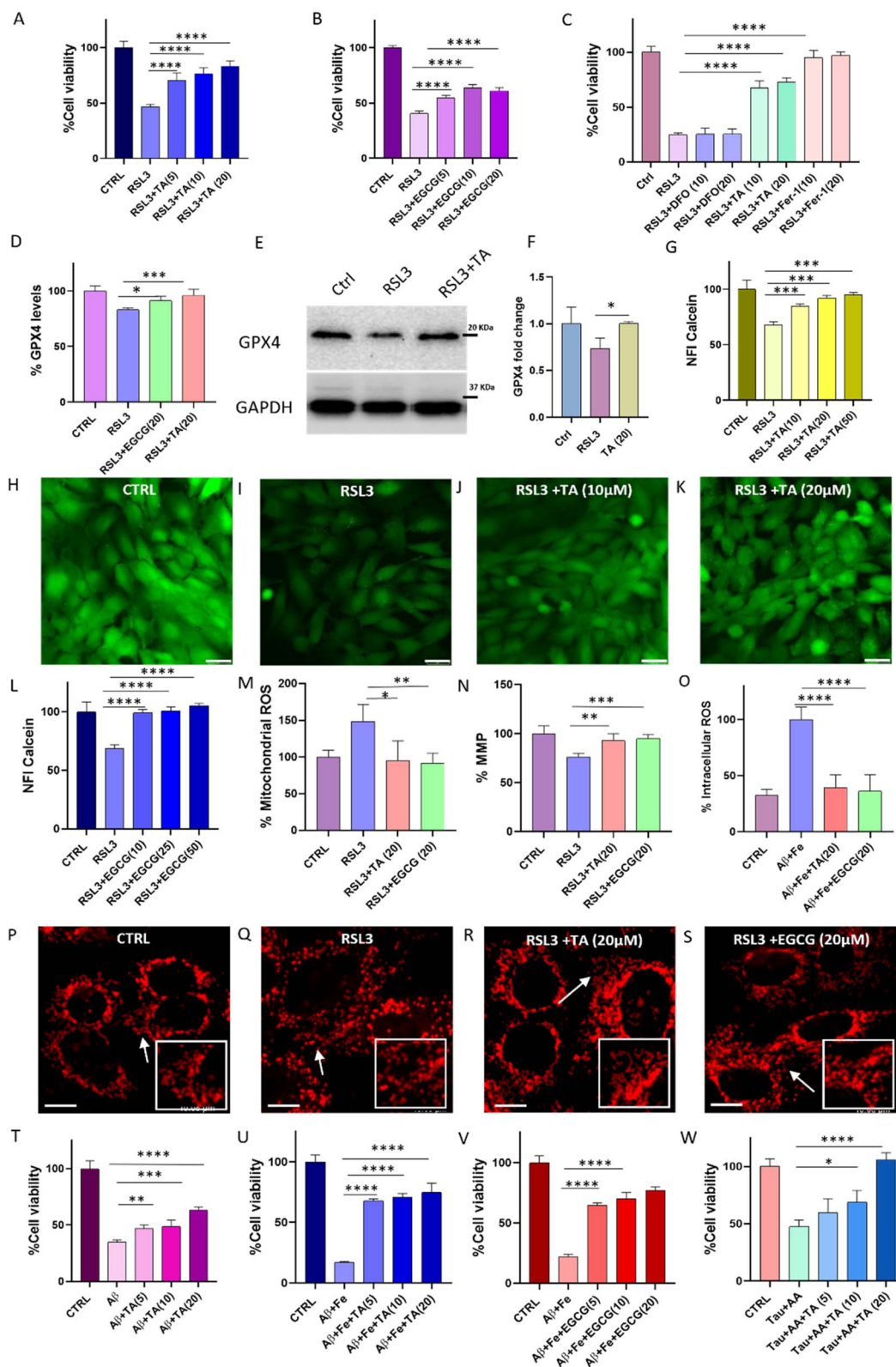


Fig. 5 Studies in cells show the ability of TA and EGCG to rescue neuronal cells from ferroptosis and A β_{42} -induced toxicity. The numbers in the parentheses represent the concentration of the compounds in μM . Neuronal cell rescue from RSL3 (500 nM) induced ferroptosis by (A) TA and (B) EGCG, (C) comparative study with ferrostatin and DFO, (D) immunofluorescence (IF) study to monitor relative GPX4 levels in cells treated with RSL3 (1 μM) alone and in the presence of TA (20 μM) and EGCG (20 μM), and (E) western blot and its quantification to monitor GPX4 levels (F) ($n > 3$). (G) Monitoring LIP using calcein and visualization of LIP in (H) control, (I) RSL3 (2 μM), (J) RSL3 + TA (10 μM) and (K) RSL3 + TA (20 μM) treated cells (scale bar: 30 μm), (L) monitoring LIP in the presence of EGCG using Calcein-AM, (M) intracellular mitochondrial ROS levels monitored using MitoSOX in cells treated with RSL3 (1 μM) alone and in the presence of TA (20 μM) and EGCG (20 μM), (N) MMP monitored using Mitotracker green

EGCG, we stained the cells with calcein-acetoxymethyl ester. Calcein-acetoxymethyl ester is cleaved by esterases in cells to produce the calcein fluorophore in the cytosol, which exhibits high fluorescence.⁴⁴ However, when calcein chelates with LIP, its fluorescence is quenched, allowing for the estimation of free LIP levels. Cells treated with RSL3 (2 μM) showed an increase in intracellular Fe levels (LIP) and a corresponding decrease in the calcein fluorescence to 67%, compared to healthy cells (100%) (Fig. 5G–K). Notably, treatment with 50 μM of **TA** and **EGCG** reduced LIP levels, resulting in a corresponding increase in calcein fluorescence to approximately 95% and 100%, respectively, similar to control cells (Fig. 5L). This effect was dose-dependent and demonstrates the ability of **TA** and **EGCG** to sequester free Fe (LIP) and render it inactive. Ferroptosis triggers lipid peroxidation and increases ROS generation, leading to elevated intracellular mitochondrial ROS levels and a decreased mitochondrial membrane potential (MMP), resulting in mitochondrial fragmentation. We used a MitoSOX probe to monitor mitochondrial ROS levels in cells. RSL3 treatment (1 μM) increased mitochondrial ROS levels to 148%, compared to that in healthy cells (100%). In contrast, **TA** (20 μM) and **EGCG** (20 μM) reduced ROS levels in RSL3-treated cells to 95% and 91%, respectively, demonstrating their ability to prevent ferroptotic ROS-mediated mitochondrial damage (Fig. 5M). RSL3-induced ferroptosis and its reversal by treatment with PP was confirmed by measuring changes in MMP using rhodamine 123 (Rho123), an MMP-sensitive mitochondrial probe. The MMP of RSL3-treated cells decreased to 76%, compared to that of healthy cells (100%). However, treatment with **TA** (20 μM) and **EGCG** (20 μM) restored the MMP to 93% and 95%, respectively, indicating the prevention of functional mitochondrial damage (Fig. 5N). To assess the ability of **TA** and **EGCG** to prevent ferroptotic mitochondrial structural damage, the healthy and RSL3-treated cells were stained with Mito-TG.⁴⁵ Cells treated with RSL3 (1 μM) alone or in the presence of **TA** and **EGCG** were observed using a live cell fluorescence microscope. Healthy cells exhibited long tubular mitochondrial structures, while RSL3 treatment caused fragmentation (Fig. 5P and Q). Notably, cells treated with **TA** (20 μM) and **EGCG** (20 μM) maintained healthy tubular structures, supporting the protective role of these PPs against ferroptotic mitochondrial damage as evidenced by ROS and MMP studies (Fig. 5R and S).

Rescue of neuronal cells from amyloid-induced ferroptotic cell death

The effectiveness of **TA** and **EGCG** in modulating $\text{A}\beta_{42}$ aggregation prompted us to investigate their ability to rescue neuronal cells from $\text{A}\beta_{42}$ -induced toxicity. SH-SY5Y cells were treated with $\text{A}\beta_{42}$ alone and in the presence of **TA** and **EGCG**.

$\text{A}\beta_{42}$ (10 μM) treatment reduced cell viability to 34.8%, compared to that of untreated control cells (100%), after 30 h of incubation. However, rescue of $\text{A}\beta_{42}$ treated neuronal cells was observed in the presence of lead PPs in a dose-dependent manner, with the highest concentration of **TA** (20 μM) and **EGCG** (20 μM) increasing cell viability to 63% and 69%, respectively (Fig. 5T and S17†). In the context of ferroptosis in AD, Fe accelerates the accumulation of toxic amyloid ($\text{A}\beta_{42}$ -Fe) fibrils, generating ROS and leading to membrane damage and lipid peroxidation. We monitored the ability of **TA** and **EGCG** to modulate toxic $\text{A}\beta_{42}$ + Fe aggregation and rescue neuronal cells from $\text{A}\beta_{42}$ + Fe-induced ferroptotic cell death using MTT assay. Cell viability decreased to 17% when treated with $\text{A}\beta_{42}$: Fe (1 : 5), compared to that of untreated control cells (100%). However, treatment with **TA** (20 μM) and **EGCG** (20 μM) improved the viability of $\text{A}\beta_{42}$ + Fe treated cells to 74% and 77%, respectively, in a dose-dependent manner (Fig. 5U and V). Notably, the rescue ability of **TA** against $\text{A}\beta_{42}$ + Fe-induced toxicity was higher than that of $\text{A}\beta_{42}$ toxicity and comparable to the modulation ability of **EGCG** against $\text{A}\beta_{42}$ + Fe toxicity. This supports the results from ThT studies where **TA** was found to have a superior ability to modulate $\text{A}\beta_{42}$ aggregation in the presence of Fe compared to $\text{A}\beta_{42}$ alone. The ability of **TA** and **EGCG** as potent antioxidants in cells was investigated by monitoring intracellular ROS levels in the presence of H_2O_2 and $\text{A}\beta_{42}$ + Fe independently using 2',7'-dichlorodihydrofluorescein diacetate (DCFDA). Treatment with **TA** (20 μM) and **EGCG** (20 μM) reduced ROS in H_2O_2 -treated cells to 34% and 51%, respectively, compared to H_2O_2 treated cells (100%), indicating their ability to quench intracellular ROS (Fig. S18†). Cells were incubated with $\text{A}\beta_{42}$ + Fe alone and in the presence of **TA** and **EGCG**, and intracellular ROS levels were monitored using DCFDA. $\text{A}\beta_{42}$ + Fe (1 : 5) increased intracellular ROS to 100%, compared to 31% for untreated cells, after 6 h incubation. However, treatment with **TA** (20 μM) and **EGCG** (20 μM) reduced ROS levels in $\text{A}\beta_{42}$ + Fe treated cells to 36% and 38%, respectively, indicating their ability to complex and render Fe redox-inactive, modulate the $\text{A}\beta_{42}$ -Fe Fenton-type reaction, and ultimately prevent ROS generation (Fig. 5O). These cellular studies strongly support the ability of **TA** and **EGCG** to alleviate RSL3-induced ferroptosis and $\text{A}\beta_{42}$ -Fe-associated toxicity, making them potential candidates for synergistically targeting both ferroptosis and AD. In conjunction with ThT studies, we evaluated **TA**'s ability to protect neuronal cells from tau-induced toxicity. In the presence of AA-induced tau aggregates, cell viability decreased to 47%, compared to that of healthy cells (100%) (Fig. 5W). A dose-dependent increase in cell viability was observed with **TA** (20 μM), increasing the cell viability to 100%.

To corroborate the connection between $\text{A}\beta_{42}$ and ferroptosis, an immunofluorescence assay was performed to measure GPX4

in cells treated with RSL3 (1 μM) alone and in the presence of **TA** (20 μM) and **EGCG** (20 μM), (O) DCFDA assay to monitor intracellular ROS in cells treated with $\text{A}\beta_{42}$: Fe (1 : 5), and in the presence of **TA** (20 μM) and **EGCG** (20 μM). Mitochondrial fragmentation monitored using MitoTG (500 nM) in (P) healthy cells, and cells treated with (Q) RSL3 (1 μM), (R) RSL3 (1 μM) + **TA** (20 μM) and (S) RSL3 (1 μM) + **EGCG** (20 μM) (scale bar: 10 μm). Concentration-dependent study of $\text{A}\beta_{42}$ (10 μM) induced toxicity and rescue by (T) **TA**, $\text{A}\beta_{42}$: Fe (1 : 5) induced toxicity and its rescue with (U) **TA** and (V) **EGCG**, and (W) AA-induced tau (5 μM) toxicity and rescue by **TA** (μM). (the experiment was repeated at least in triplicate, and statistics was applied with one-way ANOVA; * p = 0.05).



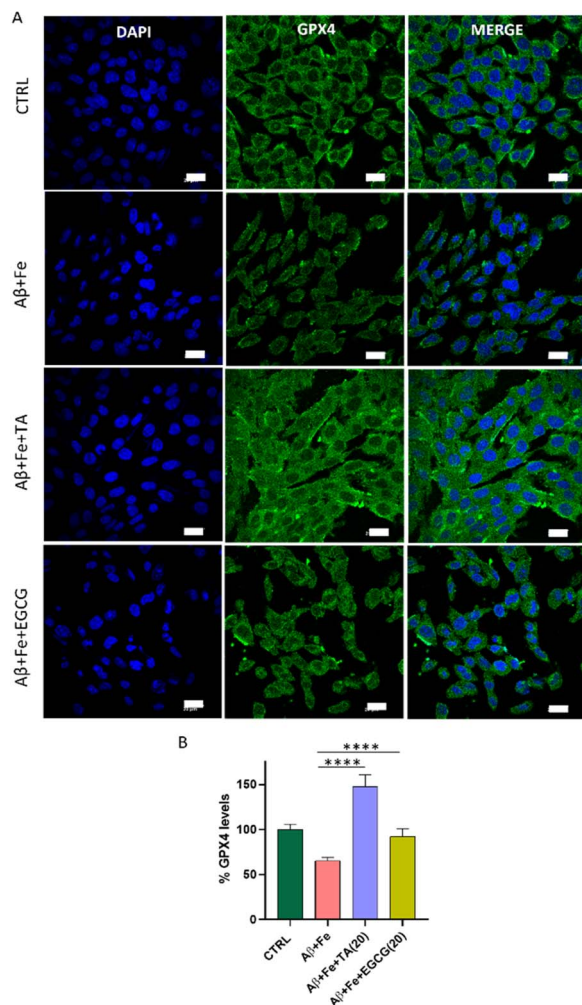


Fig. 6 Protein quantification performed via immunofluorescence (IF) assay. The numbers in the parentheses represent the concentration of the compounds in μM . (A) IF imaging to monitor the GPX4 levels, in the presence of $\text{A}\beta_{42}:\text{Fe}$ (1:5) treated cells independently and in the presence of TA (20 μM) and EGCG (20 μM), and its (B) quantification (over 200 cells were quantified and statistics was applied with one-way ANOVA; $*p = 0.05$) (scale bar: 20 μm).

levels in the SH-SY5Y neuronal cell lines incubated with $\text{A}\beta_{42} + \text{Fe}$ alone and in the presence of TA and EGCG. Treatment of cells with $\text{A}\beta_{42} + \text{Fe}$ (1:5) for 30 h significantly reduced GPX4 levels to 65%, compared to that of healthy cells (100%) (Fig. 6). To our knowledge, this is the first report of a direct correlation between $\text{A}\beta_{42} + \text{Fe}$ and GPX4 levels in neuronal cells in the context of ferroptosis, as determined by the immunofluorescence assay that directly quantifies protein levels. Remarkably, TA substantially increased the GPX4 levels to 147% in $\text{A}\beta_{42} + \text{Fe}$ treated cells compared to in untreated control cells (100%), indicating that TA can elevate GPX4 levels under AD pathological conditions.

These findings prompted us to examine TA as a GPX4 enhancer in neuronal cells. In consistence with the above study, we observed an increase in intracellular GPX4 levels to 192% in TA-treated cells compared to that in untreated cells (100%)

(Fig. 7A and B). This supports our assertion that TA not only enhances GPX4 activity but also increases its levels in cells. Furthermore, western blot analysis was performed to quantify GPX4 levels. The results revealed that TA treatment increased GPX4 levels to 127% compared to that in untreated cells (100%) supporting our earlier observation (Fig. 7C, D and S21[†]). Intrigued by these findings, we examined changes in the antioxidant master regulator nuclear factor erythroid 2-related factor 2 (Nrf2), which is known to, directly and indirectly, regulate GPX4 and its associated antioxidant proteins.⁴⁶ While there are reports indicating the ability of TA to activate the Nrf2 pathway, we assessed Nrf2 activation upon treatment with TA in neuronal cells.^{47,48} Study revealed that the treatment with TA resulted in Nrf2 accumulation and nuclear translocation in SH-SY5Y cells. Intracellular Nrf2 levels increased to 148% compared to that in untreated cells (100%), and there was a 2-fold nuclear translocation of the Nrf2 protein from the cytoplasm upon treatment with TA (20 μM) (Fig. 7E–G). Thus, we speculate that TA enhances GPX4 levels, possibly *via* the Nrf2–GPX4 axis.

Discussion

Ferroptosis has been identified as a significant contributing factor in AD pathology, and targeting ferroptosis in conjunction with amyloid pathways through a novel and integrated approach can effectively mitigate the multifaceted AD.^{49,50} Despite emerging evidence suggesting a possible link between ferroptosis and AD, the exact nature of crosstalk remains to be elucidated and the search for dual therapeutics presents a formidable challenge. While EGCG has shown a better ability to modulate pristine $\text{A}\beta$ aggregation, TA demonstrates higher $\text{A}\beta$ aggregation modulating ability in the presence of Fe. Although, EGCG and TA showed comparable efficacy in most of the other studies, TA eventually emerged as the lead candidate in the context of ferroptosis due to its binding to the activator site of GPX4, a selenoenzyme and master regulator of the conversion of toxic lipid peroxides to lipid alcohol. The reduced GPX4 levels by $\text{A}\beta_{42}$ –Fe demonstrate the interplay between amyloid toxicity and ferroptosis and may provide the missing link between AD and ferroptosis. Remarkably, TA acts as an activator of GPX4 and enhances its intracellular protein levels even under AD pathological conditions. Despite ongoing efforts to identify ferroptosis inhibitors, advancements in the activation axis of GPX4 are still in their infancy. Fe-chelators and lipid ROS scavengers are less selective than GPX4 activators in suppressing ferroptosis mainly because GPX4 inhibition is a direct characteristic feature of ferroptosis.⁴¹ While selenium has been utilized to stimulate GPX4 activity and few small molecule GPX4 activators have been reported,^{41,42} to the best of our knowledge, this is the first report identifying a single multifunctional molecule as a GPX4 activator and enhancer of its levels that can also work *via* Fe-chelation and radical trapping mechanisms. The discovery of a natural polyphenol, TA as a GPX4 activator that ameliorates $\text{A}\beta$ induced ferroptosis holds great significance and this study presents new opportunities for the synergistic inhibition of ferroptosis in AD.



Fig. 7 Protein quantification performed via IF assay and western blotting. (A) Relative GPX4 levels monitored via IF assay with TA (20 μM) and its (B) quantification. (C) Western blot to monitor GPX4 in the presence of TA and its corresponding quantification ($n > 3$) (D). (E) Nrf2 activation by TA (20 μM) leading to its (F) accumulation and (G) nuclear translocation (over 200 cells were quantified or $N > 3$ and the statistics was performed with Student's *t*-test with **** $P < 0.0001$) (scale bar: 30 μm).

GPX4 levels are modulated by various transcriptional factors such as Nrf2, mechanistic target of rapamycin complex 1 (mTORC1), and twelve channel transmembrane protein transporter vector family 7 member 11 (SLC7A11)-mediated cystine transport, among others. Nrf2 regulates the synthesis of GPX4-related enzymes including glucose-6-phosphate dehydrogenase (G6PD), GSH and its reductase, glutamate–cysteine ligase modifier subunit (GCLM), thioredoxin reductase 1, SLC711, glutamate–cysteine ligase catalytic subunit, and the peroxisome proliferator activator receptor gamma pathway.⁵¹ Studies have shown that cyst(e)ine activates mTORC1 and promotes GPX4 protein synthesis.²⁴ Pharmacological activation of mTORC1 can increase

GPX4 protein levels. The enzymatic degradation of GPX4 is regulated by acetyl-CoA carboxylate and its inhibition can prevent GPX4 degradation.⁵² Our study demonstrated that TA activates the Nrf2 pathway in neuronal cells, leading to its accumulation and translocation to the nucleus where it activates several antioxidant response elements. Nrf2 has been studied to regulate ferroptosis based on its mechanism of action in Fe/metal metabolism, intermediate metabolism, and glutathione metabolism.⁵³ While certain pathways for the enhancement of GPX4 treated by TA have been discovered, there may be additional pathways yet to be explored that warrant further investigation. From a therapeutic perspective, TA has the ability to modulate Aβ₄₂ and tau pathways, reduce oxidative stress, aid in mitochondrial rescue, inhibit ferroptosis, and crucially activate and increase GPX4 function and levels. This positions TA as a promising candidate for the amelioration of both ferroptosis and AD, as well as addressing the liaison between them.

Conclusions

The interplay between ferroptosis and AD has been studied over the past decade. Nonetheless, the intricate nature of the mechanisms involved in both conditions presents a challenge in pinpointing a solitary factor connecting them. This study focused on Aβ₄₂-induced decrease of GPX4 enzyme levels as a major contributor to ferroptosis and a missing link with AD pathology. Despite GPX4 being a key regulator of ferroptosis, therapeutic approaches targeting GPX4 activation to combat ferroptosis remain largely unexplored and unsuccessful. In this work, we discover that the natural polyphenol TA is a highly effective inhibitor of ferroptosis. It acts through all major routes of ferroptosis, including Fe-chelation, inhibition of lipid peroxidation, rescue of mitochondrial damage, and activation of the Nrf2–GPX4 axis, thereby augmenting their levels. Concurrently, TA acts as a potent inhibitor of Aβ₄₂ and tau aggregation and effectively modulates highly toxic Fe-induced Aβ₄₂ aggregation, reduces oxidative stress, and combats Fe-dyshomeostasis in AD. While GPX4 protein synthesis is highly inefficient and energetically demanding, we demonstrated how a natural polyphenol (TA), offers a viable solution to synergistically modulate the multifaceted toxicity of both ferroptosis and AD, with GPX4 activation as one of the crucial mechanisms. This may encourage researchers to explore nontoxic natural products for solutions and underscore the significance of GPX4 in effectively modulating ferroptosis as well as elucidating its role in AD.

Data availability

All experimental data are available within the article and the ESI.†

Author contributions

T. G. conceptualized the project; P. B., H. H. and T. G. designed the experiments; P. B. and H. H. contributed equally; P. B. performed *in vitro* and *in silico* studies; H. H., M. R. and D. P. performed cellular studies; all authors contributed to curating



and analysing the data; P. B., H. H. and T. G. wrote the manuscript, and others gave inputs.

Conflicts of interest

There are no conflicts to declare.

Acknowledgements

The authors thank JNCASR, core grant (CRG/2020/004594), Science and Engineering Research Board (SERB), New Delhi, India, for the funding. HH, MR, and DP thank CSIR, UGC and DST, India for the student fellowships.

References

- 1 Alzheimer's Association, *Alzheimers Dement.*, 2022, **18**, 700–789.
- 2 J. Hardy and D. Selkoe, *Science*, 2002, **297**, 353–356.
- 3 *Alzheimer's Disease: Recent Findings in Pathophysiology, Diagnostic and Therapeutic Modalities*, ed. T. Govindaraju, The Royal Society of Chemistry, London, 2022.
- 4 K. J. Brnham, C. L. Masters and A. I. Bush, *Nat. Rev. Drug Discovery*, 2004, **3**, 205–214.
- 5 D. M. Holtzman, J. C. Morris and A. M. Goate, *Sci. Transl. Med.*, 2011, **3**, 77.
- 6 Y. Liu, M. Nguyen, A. Robert and B. Meunier, *Acc. Chem. Res.*, 2019, **52**, 2026–2035.
- 7 D. A. Butterfield and B. Halliwell, *Nat. Rev. Neurosci.*, 2019, **20**, 148–160.
- 8 G. B. Frisoni, D. Altomare, D. R. Thal, F. Ribaldi, R. van der Kant, R. Ossenkoppele, K. Blennow, J. Cummings, C. van Duijn, P. M. Nilsson, P.-Y. Dietrich, P. Scheltens and B. Dubois, *Nat. Rev. Neurosci.*, 2022, **23**, 53–66.
- 9 L. Zecca, M. B. H. Youdim, P. Riederer, J. R. Connor and R. R. Crichton, *Nat. Rev. Neurosci.*, 2004, **5**, 863–873.
- 10 M. Ramesh and T. Govindaraju, *Chem. Sci.*, 2022, **13**, 13657–13689.
- 11 J. Seigny, P. Chiao, T. Bussière, P. H. Weinreb, L. Williams, M. Maier, R. Dunstan, S. Salloway, T. Chen, Y. Ling, J. O'Gorman, F. Qian, M. Arastu, M. Li, S. Chollate, M. S. Brennan, O. Quintero-Monzon, R. H. Scannevin, H. M. Arnold, T. Engber, K. Rhodes, J. Ferrero, Y. Hang, A. Mikulskis, J. Grimm, C. Hock, R. M. Nitsch and A. Sandrock, *Nature*, 2016, **537**, 50–56.
- 12 C. J. Swanson, Y. Zhang, S. Dhadda, J. Wang, J. Kaplow, R. Y. K. Lai, L. Lannfelt, H. Bradley, M. Rabe, A. Koyama, L. Reyderman, D. A. Berry, S. Berry, R. Gordon, L. D. Kramer and J. L. Cummings, *Alzheimer's Res. Ther.*, 2021, **13**, 80.
- 13 S. J. Dixon, K. M. Lemberg, M. R. Lamprecht, R. Skouta, E. M. Zaitsev, C. E. Gleason, D. N. Patel, A. J. Bauer, A. M. Cantley, W. S. Yang, B. Morrison 3rd and B. R. Stockwell, *Cell*, 2012, **149**, 1060–1072.
- 14 J. Dixon and B. R. Stockwell, *Nat. Chem. Biol.*, 2014, **10**, 9–17.
- 15 S. Doll and M. Conrad, *IUBMB Life*, 2017, **69**, 423–434.
- 16 B. R. Stockwell, *Cell*, 2022, **185**, 2401–2421.
- 17 X. Jiang, B. R. Stockwell and M. Conrad, *Nat. Rev. Mol. Cell Biol.*, 2021, **22**, 266–282.
- 18 D. Chen, B. Chu, X. Yang, Z. Liu, Y. Jin, N. Kon, R. Rabadan, X. Jiang, B. R. Stockwell and W. Gu, *Nat. Commun.*, 2021, **12**, 3644–3649.
- 19 L. Rochette, G. Dogon, E. Rigal, M. Zeller, Y. Cottin and C. Vergel, *Int. J. Mol. Sci.*, 2023, **24**, 449.
- 20 G. Lei, L. Zhuang and B. Gan, *Nat. Rev. Cancer*, 2022, **22**, 381–396.
- 21 H. Wood, *Nat. Rev. Neurol.*, 2015, **11**, 369–372.
- 22 Y. Zhang, M. Wang and W. Chang, *Front. Pharmacol*, 2022, **13**, 983623.
- 23 S. Ayton, N. G. Faux and A. I. Bush, *Nat. Commun.*, 2015, **6**, 6760.
- 24 J. Chen, L. Yang, L. Geng, J. He, L. Chen, Q. Sun, J. Zhao and X. Wang, *Front. Cell. Neurosci.*, 2021, **15**, DOI: [10.3389/fncel.2021.632354](https://doi.org/10.3389/fncel.2021.632354).
- 25 W. S. Hambricht, R. S. Fonseca, L. Chen, R. Na and Q. Ran, *Redox Biol.*, 2017, **12**, 8–17.
- 26 W.-D. Bao, P. Pang, X.-T. Zhou, F. Hu, W. Xiong, K. Chen, J. Wang, F. Wang, D. Xie, Y.-Z. Hu, Z.-T. Han, H.-H. Zhang, W.-X. Wang, P. T. Nelson, J.-G. Chen, Y. Lu, H.-Y. Man, D. Liu and L.-Q. Zhu, *Cell Death Differ.*, 2021, **28**, 1548–1562.
- 27 L. Cong, X. Dong, Y. Wang, Y. Deng, B. Li and R. Dai, *Eur. J. Med. Chem.*, 2019, **166**, 11–21.
- 28 Y. Zhang, R. V. Swanda, L. Nie, X. Liu, C. Wang, H. Lee, G. Lei, C. Mao, P. Koppula, W. Cheng, J. Zhang, Z. Xiao, L. Zhuang, B. Fang, J. Chen, S.-B. Qian and B. Gan, *Nat. Commun.*, 2021, **12**, 1589.
- 29 S. Samanta, K. Rajasekhar, V. Babagond and T. Govindaraju, *ACS Chem. Neurosci.*, 2019, **10**, 3611–3621.
- 30 K. Rajasekhar, R. Madhu and T. Govindaraju, *ACS Chem. Neurosci.*, 2016, **7**, 1300–1310.
- 31 D. Padhi, C. Balachandra, M. Ramesh and T. Govindaraju, *Chem. Commun.*, 2022, **58**, 6288–6291.
- 32 K. Rajasekhar, S. Samanta, V. Bagoband, N. A. Murugan and T. Govindaraju, *iScience*, 2020, **23**, 101005.
- 33 M. Konar, D. Ghosh, S. Samanta and T. Govindaraju, *RSC Chem. Biol.*, 2022, **3**, 220–226.
- 34 M. Deleanu, J.-F. Hernandez, L. Cipelletti, J.-P. Biron, E. Rossi, M. Taverna, H. Cottet and J. Chamieh, *Anal. Chem.*, 2021, **93**, 6523–6533.
- 35 L. S. Stelzl, L. M. Pietrek, A. Holla, J. Oroz, M. Sikora, J. Köfinger, B. Schuler, M. Zweckstetter and G. Hummer, *JACS Au*, 2022, **2**, 673–686.
- 36 D. Tang, X. Chen, R. Kang and G. Kroemer, *Cell Res.*, 2021, **31**, 107–125.
- 37 W. S. Yang, K. J. Kim, M. M. Gaschler, M. Patel, M. S. Shchepinov and B. R. Stockwell, *Proc. Natl. Acad. Sci. U. S. A.*, 2016, **113**, 4966–4975.
- 38 M. Weiwer, J. A. Bittker, T. A. Lewis, K. Shimada, W. S. Yang, L. MacPherson, S. Dandapani, M. Palmer, B. R. Stockwell, S. L. Schreiber and B. Munoz, *Bioorg. Med. Chem. Lett.*, 2012, **22**, 1822–1826.
- 39 W. S. Yang and B. R. Stockwell, *Chem. Biol.*, 2008, **15**, 234–245.



- 40 S. Li, Y. He, K. Chen, J. Sun, L. Zhang, Y. He, H. Yu and Q. Li, *Oxid. Med. Cell. Longevity*, 2021, **2021**, 2915019.
- 41 C. Li, X. Deng, X. Xie, Y. Liu, J. P. F. Angeli and L. Lai, *Front. Pharmacol.*, 2018, **9**, 1120.
- 42 C. Li, X. Deng, W. Zhang, X. Xie, M. Conrad, Y. Liu, J. P. F. Angeli and L. Lai, *J. Med. Chem.*, 2019, **62**, 266–275.
- 43 B. R. Stockwell, J. P. F. Angeli, H. Bayir, A. I. Bush, M. Conrad, S. J. Dixon, S. Fulda, S. Gascón, S. K. Hatzios, V. E. Kagan, K. Noel, X. Jiang, A. Linkermann, M. E. Murphy, M. Overholtzer, A. Oyagi, G. C. Pagnussat, J. Park, Q. Ran, C. S. Rosenfeld, K. Salnikow, D. Tang, F. M. Torti, S. V. Torti, S. Toyokuni, K. A. Woerpel and D. D. Zhang, *Cell*, 2017, **171**, 273–285.
- 44 F. Thomas, G. Serratrice, C. Béguin, E. Saint Aman, J. L. Pierre, M. Fontecave and J. P. Laulhère, *J. Biol. Chem.*, 1999, **274**, 13375–13383.
- 45 M. Ramesh, K. Rajasekhar, K. Gupta, V. Babagond, D. K. Saini and T. Govindaraju, *Org. Biomol. Chem.*, 2021, **19**, 801–808.
- 46 M. Dodson, R. Castro-Portuguez and D. D. Zhang, *Redox Biol.*, 2019, **23**, 101107.
- 47 M. Li, P. Liu, Y. Xue, Y. Liang, J. Shi, X. Han, J. Zhang, X. Chu and L. Chu, *Oncol. Rep.*, 2020, **44**, 2306–2316.
- 48 W. Jin, Y. Xue, Y. Xue, X. Han, Q. Song, J. Zhang, Z. Li, J. Cheng, S. Guan, S. Sun and L. Chu, *Biomed. Pharmacother.*, 2020, **126**, 110047.
- 49 M. A. Greenough, D. J. R. Lane, R. Balez, H. T. D. Anastacio, Z. Zeng, K. Ganio, C. A. McDevitt, K. Acevedo, A. A. Belaidi, J. Koistinaho, L. Ooi, S. Ayton and A. I. Bush, *Cell Death Differ.*, 2022, **29**, 2123–2136.
- 50 B. R. Stockwell and X. Jiang, *Cell Chem. Biol.*, 2020, **27**, 365–375.
- 51 P. Koppula, L. Zhuang and B. Gan, *Protein Cell*, 2021, **12**, 599–620.
- 52 K. Shimada, R. Skouta, A. Kaplan, W. S. Yang, M. Hayano, S. J. Dixon, L. M. Brown, C. A. Valenzuela, A. J. Wolpaw and B. R. Stockwell, *Nat. Chem. Biol.*, 2016, **12**, 497–503.
- 53 X. Song and D. Long, *Front. Neurosci.*, 2020, **14**, 267.

